CHEMELECTROCHEM
Articles

Special Collection

Synchronous Electrical Conductance- and Electron Tunnelling-Scanning Electrochemical Microscopy Measurements

James F. Edmondson,[a, b] Gabriel N. Meloni,[a] Giovanni Costantini,*[a] and Patrick R. Unwin*[a]

Dedicated to Dick Crooks on the occasion of his 65th birthday and in recognition of his science, support and friendship

The requirement to separate topographical effects from surface electrochemistry information is a major limitation of scanning electrochemical microscopy (SECM). With many applications of SECM involving the study of (semi)conducting electrode surfaces, the hybridisation of SECM with scanning tunnelling microscopy (STM) or a surface conductance probe would provide the ultimate topographical imaging capability to SECM, but previous attempts are limited. Here, the conversion of a general scanning electrochemical probe microscopy (SEPM) platform to facilitate contact electrical conductance (C)- and electron tunnelling (T)-SECM measurements is considered. Measurements in air under ambient conditions with a Pt/Ir wire tip are used to assess the performance of the piezoelectric positioning system. A hopping-mode imaging protocol is implemented, whereby the tip approaches the surface at each pixel until a desired current magnitude is exceeded, and the corresponding z position (surface height) is recorded at a set of predefined xy coordinates in the plane of the surface. At slow tip approach rates, the current shows an exponential dependence on tip-substrate distance, as expected for electron tunnelling. For measurements in electrochemical environments, in order to overcome well-known problems with leakage currents at coated-wire tips used for electrochemical STM, Pt-sensitised carbon nanoelectrodes are used as tips. The hydrogen evolution reaction on 2D Au nanocrystals serves as an exemplar system for the successful simultaneous mapping of topography and electrochemical activity.

1. Introduction

The invention of the scanning tunnelling microscope (STM)[1] had a significant impact on the study of electrochemical interfaces and further led to the development of electrochemically-based scanned probe microscopes (SPMs).[2–9] Scanning electrochemical probe microscopes (SEPMs), which use a small electrode or electrochemical half-cell as a probe (tip), have attracted considerable attention as a means of mapping electrochemical activity and chemical fluxes at the microscale and nanoscale for a wide range of substrates and materials.[3–5,10–16] While the spatiotemporal resolution of SEPM has improved over the years, the ultimate lateral resolution of these methods is generally limited by either diffusion of the measured species to the electrode (diffusional blur) and/or the physical size of the tip used.[17]

A well-known problem of some SEPMs, like scanning electrochemical microscopy (SECM), is that the tip response depends on both surface activity and tip-substrate distance. This issue is compounded because the technique mainly operates in a constant height imaging mode, without positional feedback of the tip, which makes imaging at the nanoscale particularly challenging.[18] To overcome these limitations, SECM has been combined with other SPM techniques, in order to provide independent (unambiguous) topography and activity measurements, with positional feedback usually implemented so that the probe traces the surface topography.[13,19–22] Particular successes include the combination of SECM with atomic force microscopy (AFM),[20,23–25] scanning ion conductance microscopy (SICM),[26,27] shear force microscopy[28] and the use of potential-pulse imaging methods, implemented on both SECM and SICM formats.[14,29,30]

The combination of liquid-phase (*in-situ* electrochemical) STM with SECM is particularly attractive, as the tip for both techniques is an electrically conductive wire, insulated except at the very end of the tip.[21,22,31] STM is capable of mapping surface structure with atomic resolution[32] and provides a sample to tip separation (to within the tunnelling distance, ca. 2 nm) for implementation with SECM measurements.[21,22] Despite these key features, reports of STM-SECM have been somewhat limited. Older applications of STM-SECM relied on acquiring topography and electrochemical information asynchronously, in separate scans,[21,22] which requires there to be minimal drift of

[a] J. F. Edmondson, Dr. G. N. Meloni, Prof. G. Costantini, Prof. P. R. Unwin
Department of Chemistry
University of Warwick
Gibbet Hill Road, Coventry, CV4 7AL UK
E-mail: G.Costantini@warwick.ac.uk
P.R.Unwin@warwick.ac.uk
[b] J. F. Edmondson
MAS CDT
University of Warwick
Senate House, Gibbet Hill Road, Coventry, CV4 7AL UK

Special Collection An invited contribution to the Richard M. Crooks Festschrift

the tip and sample between the STM and SECM scans on the imaging time frame, which can be lengthy, especially for SECM. Additionally, in some previous reports, leakage currents at the etched wire tips were too high to enable sufficiently accurate electrochemical measurements, and the probe geometry was difficult to elucidate.[33–35] More recently, tunnelling currents were reported during conventional nanoscale SECM imaging and SECM approach curve measurements (where the tip was translated towards a surface or nanoparticle on an insulating support) at close tip-substrate separations on a conventional SECM instrument.[36–38]

Here, we consider the conversion of a state-of-the-art SEPM instrument to enable electrical conductance (C)- and electron tunnelling (T)-SECM measurements, as a simple means of obtaining topography-electrochemical activity maps. A "tip hopping-potential pulse" scanning pattern is implemented (Figure 1), where the tip is approached to the sample at a series of predefined points across the surface (in a hopping mode). For the conductance and tunnelling (topography) measurements, the sample electrode is poised at a potential where there is no electrochemical reaction, and once the tip reaches the (near) surface region (tip current threshold exceeded and topography recorded), the tip is withdrawn slightly and the substrate potential is stepped to a value to drive an electrochemical reaction for SECM measurements at the tip. Such a tip hopping-potential pulse format has been used recently by our group for SICM measurements of topography and activity.[14] To demonstrate the C- and T-SECM setup, we consider the hydrogen evolution reaction (HER) on 2D Au nanocrystals supported

on a glassy carbon (GC) electrode, for which we have recently reported nanoscale scanning electrochemical cell microscopy (SECCM) topography-activity measurements.[39] We also report tunnelling and conductance current measurements in air to examine key factors that need to be considered when attempting to make conductance or STM-related measurements on an SECM platform.

2. Experimental Section

2.1. Nanoelectrode Fabrication

Given that coated wire tips[40,41] can show parasitic currents, we instead used nanopipette-based SECM probes for measurements in electrolyte solution. Quartz capillaries (QF100-50-10, Sutter Instrument Co.) were pulled to produce sharp-tapered nanopipettes, with an approx. 50 nm diameter opening at the end, using a P-2000 laser pipette puller (Sutter Instrument Co.). A two-line program was used for pulling: 1. Heat = 750, Filament = 4, Velocity = 30, Delay = 150, Pull = 80, 2. Heat = 650, Filament = 3, Velocity = 40, Delay = 135, Pull = 150. Pyrolytic carbon was then deposited on the inner walls of the nanopipette, to fill the end, in a similar fashion to previous reports,[42,43] but with some automation. In short, propane/butane mixture was flowed into the rear of a pulled capillary from the non-pulled end (up to a pressure of 1.2 bar), while argon was counter-flowed continuously over the end of the nanopipette using a larger diameter capillary (QF120-90-10, Sutter Instrument Co.) with a flow rate of 0.2 L min⁻¹. While the gases were flowing, an electrically heated coil was translated along the outside of the nanopipette. The coil temperature was 750 °C, while the motion of the coil was performed by an electric stepper motor controlled by a custom controller constructed in-house (see Supporting Informa-
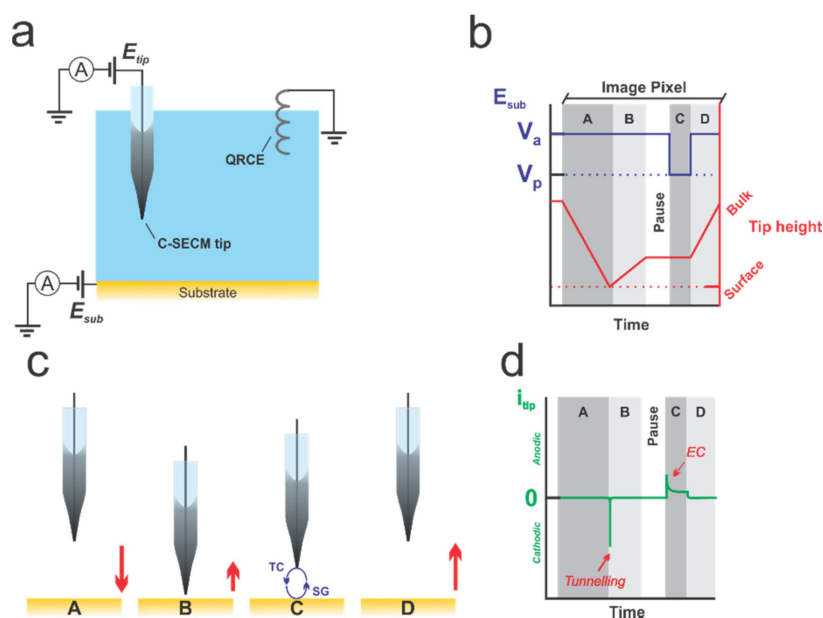

Figure 1. a) Schematic of electrode configuration for C- and T-SECM experiments, with the tip and substrate potentials controlled relative to a QRCE at ground. b,c) Schematic of potential–time for the substrate and tip, and tip position (height above substrate)-time during the "tip hopping – potential pulse" procedure. V_a is the substrate potential during approach and retract and V_p is the substrate pulse potential. The tip potential was kept constant throughout. At each pixel the tip was translated from bulk (A) towards the surface until a specific current threshold was exceeded (tunnelling/conductance mode), with the resulting (*xyz*) co-ordinates used for topography mapping (B). After a small retract of the tip, the tip current during the subsequent substrate potential pulse was used for electrochemical activity mapping in the substrate generation/tip collection (SG/TC) mode (C), before the probe was moved back to bulk (D) and then translated laterally to record data at the next predefined pixel. d) Expected tip current (i_{tip}) during the experimental protocol highlighting the tunnelling and electrochemical (EC) currents.

tion, Section SI-1). An electrical connection to the carbon deposit was made by inserting a copper wire into the back of the nanopipette so that it made physical contact with the carbon.

The final step of fabrication of SECM tips involved the potentiodynamic electrodeposition of Pt onto the carbon nanoelectrode, by adapting a method previously reported.[44] This step served 2 purposes to: (i) sensitise the tip so that it could detect electrocatalytic processes (herein the detection of H_2 by electro-oxidation); and (ii) ensure that the metal electrode protruded from the end of the quartz nanopipette, essential for the tunnelling and conductance current measurements. Electrodeposition was performed using a two-electrode setup with the carbon nanoelectrode as the working electrode and an AgCl-coated Ag wire acting as a quasi-reference counter electrode (QRCE). Cyclic voltammetry (CV) measurements (scan rate of $0.2\,V\,s^{-1}$ ensuring close to steady-state conditions at the nanoscale) between $0.3\,V$ and $-0.2\,V$ in an aqueous solution containing $1\,mM$ $H_2PtCl_6\cdot 6H_2O$ (Sigma-Aldrich) and $0.1\,M$ $HClO_4$ (70%, Sigma-Aldrich) were performed repetitively until the measured current at the $-0.2\,V$ end of the sweep (enough for the reduction of platinum)[45] exceeded $50\,pA$ (Supporting Information, Figure S2a). In general, the aim was to produce a corresponding increase by a factor of ca. $\pi/2$ in the magnitude of the steady-state current for $[Ru(NH_3)_6]^{3+}$ reduction (hexaamineruthenium(III) chloride, 98%, Sigma-Aldrich, in $0.1\,M$ KCl, >99%, Sigma-Aldrich), as expected for a transition of steady-state diffusion from a planar disc to a hemispherical electrode geometry (Supporting Information, Figure S2b). Note that a hemispherical electrode is not produced by Pt electrodeposition (*vide infra*), but the change in the limiting current magnitude served as a guide as to the desired approximate electrode size. All solutions were prepared using Milli-Q water (resistivity $18.2\,M\Omega\,cm$ at $25\,^\circ C$).

Although the quality of the resulting nanoelectrode can be inferred to some extent from the electrochemical behaviour in CV experiments, estimating the electrode area by the mass-transport limiting current is equivocal,[42] because an idealised geometry has to be assumed and imperfections in the electrode can have a significant impact on mass transport and hence the diffusion-limited current. We also found that damage to the nanopipette during the carbon deposition process sometimes resulted in Pt deposition in locations other than the end of the probe. Such electrodes had non-ideal geometries, and could not be used for imaging, but still displayed the sigmoidal voltammetry profile expected for steady-state diffusion to a nanoelectrode (Supporting Information, Figure S3). The use of high resolution microscopy techniques was essential to ensure thorough probe characterisation.[10] Herein, electrodes were characterised by both CV for $[Ru(NH_3)_6]^{3+}$ reduction (*vide supra*) and by scanning transmission electron microscopy (STEM) after imaging measurements (see, for example, Supporting Information, Figure S4). Due to the ease of fabrication and the occasional tip/substrate contact (see below), freshly made tips were used for each experiment.

2.2. 2D Au Nanocrystals and Au Nanoparticles

2D Au nanocrystals were synthesised according to previous literature.[39,46,47] 50 g lemongrass (Cymbopogon flexuosus) was finely cut and boiled in 250 mL Milli-Q water for 5 minutes. This mixture was left to cool to room temperature and 5 mL was added to 45 mL of $1\,mM$ $HAuCl_4$ (99.99%, Sigma-Aldrich). The solution was then purified by three centrifuge cycles at 3000 g and resuspended in 50 mL Milli-Q water. 2 μL of this solution was then drop cast onto a GC substrate (glassy carbon plate, 3 mm thick, type 1, 25×25 mm, Alfa Aesar), followed by washing with Milli-Q water. The drop cast area was masked off using tape (3 M

Polyimide) to leave a disc-shaped electrode of approximately 2 mm diameter exposed area.

A solution of AuNPs (gold nanoparticles, 200 nm diameter, stabilised in citrate buffer, Sigma-Aldrich) was diluted 20 fold before sonicating for 20 minutes. 1 μL of this solution was then drop cast onto a GC support (glassy carbon plate, 3 mm thick, type 1, 25×25 mm, Alfa Aesar). The GC was washed with water to remove any salt residue before experiments.

2.3. SPM Instrumentation

All SPM experiments were performed on an apparatus constructed in-house. Motion control of the tips was performed by piezoelectric positioners with accompanying amplifiers, all from Physik Instrumente. Vertical probe translation along the axis perpendicular to the substrate (z) was performed by a P-753.1CD actuator controlled by an E665 unit. Lateral translation in the substrate plane (xy) relied on a P-733.2DD actuator controlled by two E505 units and an E509 signal conditioning unit mounted on a single rack. For all axes movement, commands and position reading were performed by analog interfaces using a 16-bit FPGA card. Comparison tests were made with other positioners and controllers (*vide infra*). Coarse lateral and vertical motion was carried out using "Picomotor" linear actuators (Newport), the properties of which have been assessed elsewhere,[48] and which cause no detectable additional positioning noise when locked compared to manual micrometer positioners.

Ambient (in air) experiments used a Pt/Ir wire tip (70/30%, 0.25 mm diameter, Sigma-Aldrich) mechanically cut at one end and connected to copper wire at the other, and the substrate was connected to ground. All conductance and tunnelling current experiments in an electrochemical environment were performed in a three-electrode system with the tip (Pt nanoelectrode) and substrate (small area GC, *vide supra*) acting as working electrodes, and an Ag/AgCl QRCE (Figure 1a). Potentials were applied to, and the current measured at, both the tip and substrate electrodes using separate electrometers built in house, with all potentials reported with respect to the Ag/AgCl QRCE. Care was taken to ensure that the current at the substrate was sufficiently small (*vide infra*) so that a QRCE could be used rather than separate counter and reference electrodes.

Control of the instrument and data acquisition was achieved using an FPGA card (PCIe-7825R, National Instruments) with home designed LabVIEW software (WEC-SPM).[49] The piezoelectric components, and the cell containing the substrate electrode, tip and QRCE were kept inside a Faraday cage on a vibration isolation table (Newport S-2000 series pneumatic vibration isolators). With the cage closed, thermal drift of the positioning system was minimised by employing aluminium heatsinks (increased thermal inertia) and vacuum isolation panels as liners inside the Faraday cage.[50] The electronics (controllers, amplifiers etc.) were placed on a separate shelf in order to isolate any associated vibrations. The vibration isolation capacity of the system was assessed using a speaker as an acoustic noise generator, and it was found that the system was relatively insensitive to perturbation from outside the sealed Faraday cage (see Supporting Information, SI-3, Figure S5 and associated text).

2.4. Principles of C- and T-SECM Measurements

To put our work into context, it is useful to briefly review past attempts at related measurements and describe the approach taken herein. Previous STM-SECM measurements relied on the asynchronous acquisition of STM data (used to map the sample topography) and SECM data (used to map the sample activity). In past studies,

an STM-only scan was implemented and the topography of the sample was obtained by STM constant tunnelling current imaging. After this map, an SECM experiment was performed where the tip was re-scanned over the sample, at a greater tip-substrate distance, but tracking the topography acquired previously,[22] an SPM methodology often termed "lift mode". Another study used the same method of acquiring STM topography, but then selected individual locations (nanoparticle sites) to acquire electrochemical measurements.[21] These approaches utilised typical tube piezo STM instrumentation, but will naturally be subject to tip-sample thermal drift of the holders and/or piezo-actuators between acquisition of topographical and electrochemical data. Positional drift would be even more of a concern when using SEPM instrumentation, as in recent studies where piezoelectric positioners with much larger overall ranges (100 μm) were used in a constant height mode for SECM-tunnelling current studies.[36,37,51]

The C- and T-SECM studies herein utilised the protocol portrayed in Figure 1b,c. The tip was biased with the same potential, E_{tip}, throughout the scanning procedure (with respect to the QRCE, Figure 1a) at a value where no faradaic current was expected when the tip was in bulk solution (A), but was sufficient (usually 0.4 V) to amperometrically detect electrogenerated products (electro-oxidation of H_2) from the substrate electrode reaction (when the substrate potential was pulsed to drive an electrochemical process, HER, C).[52] At each image pixel: (A) the tip was approached towards the substrate sample (bias V_a where there was no substrate reaction) until a desired current (tunnelling and/or contact) was detected; (B) immediately followed by a tip retract by a pre-set distance, followed by a pause at this position; (C) the substrate potential was then switched to a value to drive a faradaic process (V_p) and the electrogenerated products were detected at the tip, i.e. substrate generation/tip collection (SG/TC) SECM;[17] (D) finally the substrate potential was switched back to the initial value where no electrochemical reaction took place and the tip was retracted away from the surface (typically by a distance ca. 100 nm). These steps were repeated at an array of predefined pixels in a raster scan pattern to generate the final topographical and electrochemical maps. The time between pixels depended on the approach and retract speeds, pause time, potential pulse length and the time taken to translate the tip laterally between pixels (vide infra), the total for which was typically ca. 750 ms. This ensured that there was a sufficient period for the electrogenerated H_2 to diffuse away from the electrode/electrolyte interface between each measurement.

This methodology creates synchronous topographical and electrochemical maps using the z-piezoelectric position at the tip current threshold on approach and tip currents during the substrate potential pulse, respectively. It is worth noting that for the hopping scan mode, the tip approach rate is a critical parameter, as the approach must be sufficiently slow so that the electronics can react to stop the tip, but quick enough that an image can be acquired in a reasonable timeframe. Here, the response times of the following electronic components were considered for evaluating the delay in stopping the tip approach: FPGA card (1 μs), piezoelectric amplifier (10 μs), electrometer filter (200 μs), data acquisition frequency (data were acquired by averaging every 768 μs) and the resonant frequency of the piezoelectric actuator (4.8 kHz, ca. ms scale).[53] This gives an overall upper limit for the delay of ~1–2 ms (see SI, section SI-4). Given that the onset of the tunnelling current happens within ~2 nm separation between tip and substrate, the tip approach rate should be limited to ca. $<2\,\mu m\,s^{-1}$.

3. Results and Discussion

3.1. Assessment of the Stability of Piezoelectric Actuators

Commercial and purpose-designed STM instruments rely on high stability and high resolution piezoelectric actuators and controllers, coupled with the use of appropriate vibration and thermal isolation systems. Such positioning systems often make use of tube scanners that usually have limited displacement ranges ($<1\,\mu m$ vertical and $<5\,\mu m$ laterally),[54,55] constraining applications to small sample areas, which may not be appropriate for certain SECM experiments. A purpose for the studies herein was to evaluate the suitability of a general SEPM positioning system for C- and T-SECM measurements. In addition to the P-753.1CD vertical (z) piezoelectric positioner used for the main studies described, the stability and suitability of a P-621.ZCD was also tested, because this model, or models from this family, have been used in several recent nanoscale SECM studies where tunnelling currents were reported and sometimes used to modulate the tip-substrate separation.[18,36–38] Both piezoelectric actuators have a built-in capacitance sensor for measuring extension and this is also used for drift compensation. This compensation is known as "servo mode", where the output voltage of the amplifier is adjusted to keep the desired extension of the piezoelectric constant in a closed loop setup (the monitor output can be recorded regardless of servo mode use). The manufacturer-stated closed loop resolution for the P-621.ZCD and P-753.1CD positioners is 0.4 nm and 0.1 nm, respectively.[56,57] The P-621.ZCD also has a stated open loop resolution of 0.2 nm, but this is not stated for the P-753.1CD.

To investigate the stability of each actuator, a non-zero extension was set and the output from the in-built capacitive position sensor was recorded as a function of time (Figure 2), both with and without a tip mounted, with essentially the same results. Both actuators display the same discrete changes in position of at least +/−0.5 nm. The same discrete behaviour was observed for different sampling rates of the position sensor, frequencies in the range of 5 μs/data point to 1 ms/data point. Moreover, in an open loop configuration ("Servo off" mode), a piezo drift on the scale of $1\,nm\,s^{-1}$ can be observed (Figure 2), which is very significant on the tunnelling current length scale. The source of these limitations can be attributed, in part, to inherent electrical noise that is fed to the piezo controller, together with the signal, which would add to the successive discretisation error from the digital-to-analog/analog-to-digital (DA/AD) converters used.

Despite the limitations discussed above, the theoretical precision actuation of the P-753.1CD positioner is greater than the P-621.ZCD positioner due to the higher stated resolution and a much shorter overall range (15 μm vs 100 μm). Additionally, the P-753.1CD positioner also has a much higher resonant frequency (ca. 4.8 kHz)[56] compared to the P-621.ZCD (500 Hz)[57] and previous SICM work has shown that higher resonant frequency actuators have a reduced overshoot in tip approach curves (and that the overshoot is not necessarily observed in the piezoelectric monitor output).[53] Hence, the
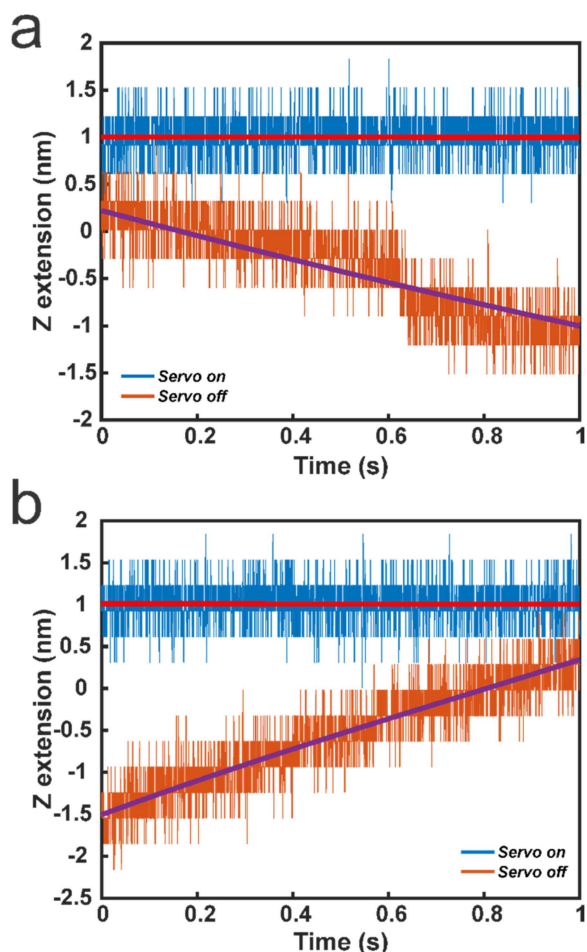
Figure 2. Readings from the in-built extension sensors over 1 second with "servo mode" on (blue) and off (orange) for the P-621.ZCD (a) and P-753.1CD (b) positioners. Both sensors exhibit a noise in position of ca. 1 nm and with the servo off, a drift on the scale of 1 nm s^{-1} is observed.

overall stability and smallest unit of motion means that the achievable resolution is higher for the P-753.1CD than the P-621.ZCD positioner. Also, the hopping methodology outlined above alleviates some of the positional instability issues as it does not require the tip to be held steady for any longer than the duration of the electrochemical pulses.

3.2. Ambient (in Air) Measurements

Given the noise in the piezoelectric monitors (*vide supra*), approach curves with a slow approach rate (2 nm s^{-1}) were plotted using the recorded time and set approach rate (converted to a distance) to avoid using the in-built piezoelectric monitors, to determine if tunnelling current measurements could be made with the instrumentation described herein. The ambient approach curve in Figure 3 shows the sensitivity achievable with a profile expected for a tunnelling approach, without a significant overshoot beyond the current threshold (30 pA). Given the slow approach rate, the onset of a non-zero current over 0.1 nm (to the last acquired data point,
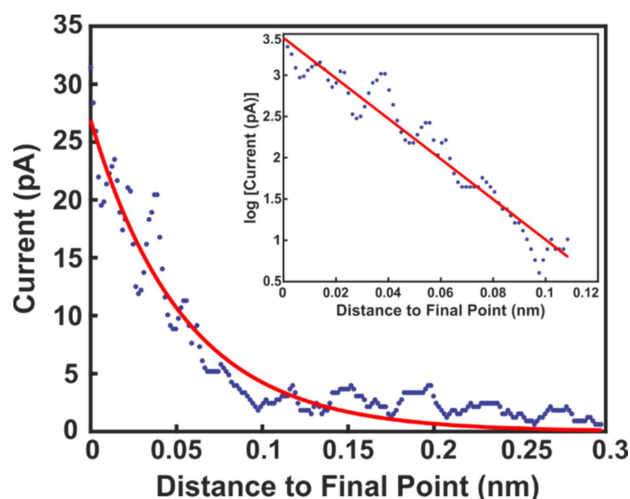

Figure 3. Approach curve with 2 nm s^{-1} approach rate and 30 pA threshold to a GC substrate, under ambient conditions, with a mechanically cut Pt/Ir wire tip. Inset shows semi-log current-distance analysis.

"Final Point") is reasonable for a tunnelling approach curve. In addition, the logarithm of the current (inset in Figure 3) shows a linear response with distance over this range, which would also be expected for a tunnelling current profile. This suggests that the instrumentation used here is potentially capable of tunnelling current measurements with very slow approach rates. For use in a hopping methodology of imaging, however, a reasonable approach rate is needed, so that scans can be obtained on a sensible time scale to avoid factors such as thermal drift and contamination of the tip and sample. Hence faster approach rates for topographical imaging were investigated (*vide infra*).

Here, we consider the possibility of using a hopping mode approach to map the topography of Au nanocrystals on a GC support, with a mechanically cut Pt/Ir wire tip. The hopping scan protocol was similar to that illustrated in Figure 1b,c, but the substrate was kept at ground throughout the experiment, with a potential applied to the tip with respect to ground, and the feedback threshold was set to 50 pA. A typical topographical scan, along with a topographical line profile is displayed in Figure 4a and 4b. As can be seen, the Au nanocrystal is readily distinguished from the substrate, presenting a height of between 10–20 nm, with respect to the support surface, which is in accord with previous measurements using SECCM and AFM.[39,58] While the spatial resolution falls short of a traditional STM instrument, this methodology evidently provides topographical data that would be highly valuable for, and complementary to, SECM (*vide supra*). Moreover, by using relatively large range actuators, the scan could be performed over a much larger area than for traditional STM scans and on samples with much greater out-of-plane topographical variations, such as Au nanoparticles on GC (Figure 4c,d).

Despite the excellent topographical resolution, it should be noted that, because of the fast tip approach rate used, there was some overshoot in the tip-sample distance in these scans. A typical approach curve from those used to generate the
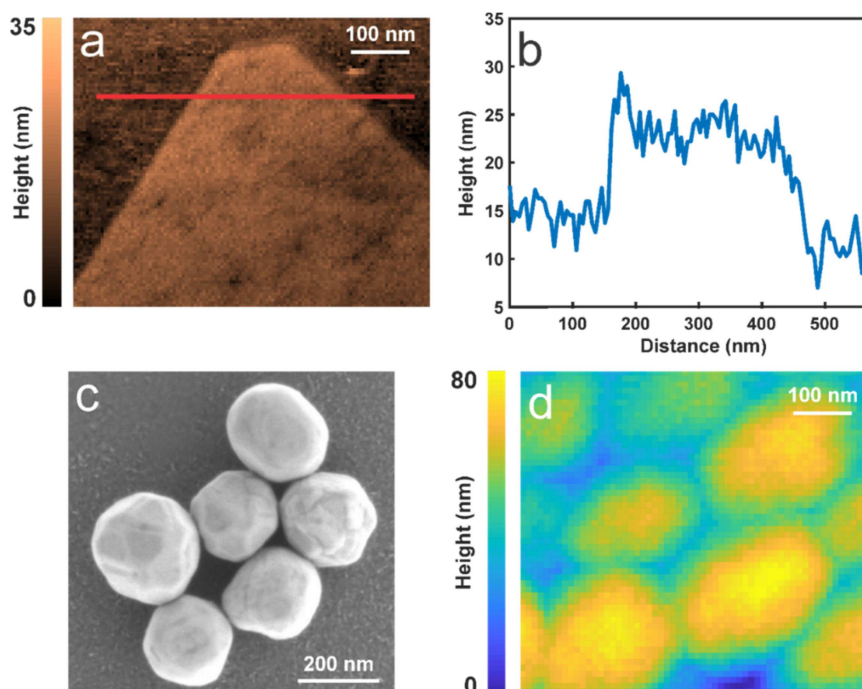
Figure 4. a) Hopping topographical imaging of a 2D Au nanocrystal on a GC surface under ambient conditions, using a mechanically cut Pt/Ir wire tip. Approach velocity: 1.1 μm s^{-1}, tip bias with respect to substrate: 0.4 V, pixel size: 5 nm, current set point: 50 pA, retract distance: 60 nm, total scan time = 24 minutes. b) Topographical profile along the red line in a). c) SEM image of drop cast 200 nm Au nanoparticles on a GC substrate. d) Hopping topographical scan of Au nanoparticles on a GC surface under ambient conditions, using a Pt/Ir wire tip. Approach velocity: 1.8 μm s^{-1}, tip bias with respect to substrate: 0.5 V, pixel size: 10 nm, current set point: 100 pA, retract distance: 250 nm, total scan time = 13 minutes. Note that there is no interpolation of topographical image data.

image in Figure 4a is shown in Figure 5a. In this case, due to the fast approach rate (1.1 μm s^{-1}), the onset of the current is usually only seen in correspondence with the one or two last data points acquired before the approach stopped (the data acquisition time was 2 ms). In order to estimate the scale of the tip position overshoot, the sample position was evaluated as discussed earlier, by multiplying the approach time by the nominal approach rate, and an exponential function (as expected for a tunnelling current) was fitted to the data points. This fitted curve was then used to calculate the position overshoot (Δz) as the difference in piezoelectric extension between the last recorded data point and the estimated point at which the current threshold was reached. This procedure was repeated for each approach curve in the scan and a histogram of the overshoot values was evaluated, as shown in Figure 5b. It can be seen that typically the overshoot is in the range of 0–2.25 nm, with a median value of 1.2 nm. This range defines the error on the z-position measurement, which is negligible compared to the surface features considered in the example cases in Figure 4. This small range also means that the tip will only just touch (or hover above) the surface in these measurements, however the range highlights how the fast hopping procedure used here is not viable for true STM measurements.

Additionally, the value of the current measured at the last point in each approach was plotted in Figure 5c, with a histogram of these values shown in Figure 5d. Here, it is interesting that higher current values are seen on the Au crystal compared to the GC. Due to the overshoot commonly being

several nm, the increased current values over Au are simply due to the higher conductivity of Au relative to GC,[59,60] indicating that some surface chemical contrast is possible from these measurements.

3.3. C-SECM in Electrolyte Solution

The ability to perform C-SECM measurements in electrolyte was investigated using the HER at Au 2D nanocrystals supported on a GC electrode (as used for one of the ambient experiments above). This system was chosen because the GC support has a much higher onset potential for HER compared to the Au nanocrystal,[61,62] and so a stark electrochemical contrast was expected. With the substrate immersed in a 0.1 M HClO$_4$ solution, a "tip hopping - potential pulse" protocol, as described above (Figure 1b,c) was employed with $V_a = 0$ V and $V_p = -0.7$ V, both against a Ag/AgCl QRCE, so as to drive the HER at the substrate (see Supporting Information, Figure S6) and allow the collection of H$_2$ (by oxidation to protons) at the tip, during the electrochemical detection period. Figure 6 shows the tip current response for the different periods (Figure 1) during an approach-retract process corresponding to one image pixel of the electrochemical maps. Initially the tip current is close to zero (in bulk). As the tip approaches the substrate, the current increases sharply in magnitude over a short time (distance), corresponding to tunnelling and/or contact with the substrate surface. Once the threshold current is attained (A), the tip
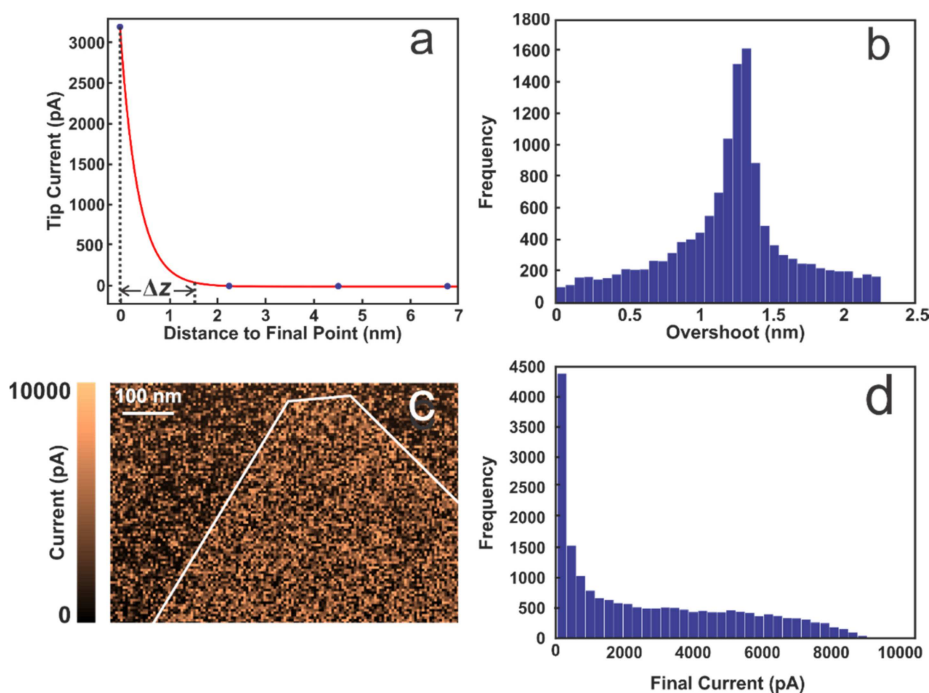
Figure 5. a) Typical approach curve taken from the hopping mode topographical scan in Figure 4a; distance is plotted using the approach rate (1.1 µm s⁻¹) and the recorded time. The overshoot in approach, Δz, is labelled and is evaluated as the difference between the final point (set as 0) and the distance at the current threshold value (50 pA). b) Histogram of all calculated overshoot values for the scan in Figure 4a. c) Same scan as in Figure 4a, showing the final tip current value in each approach. Generally, higher currents are observed over the Au nanocrystal (within the white borders, as identified from Figure 4a) compared to the GC support. d) Histogram of values from (c). Total histogram count (b and d): 13439.
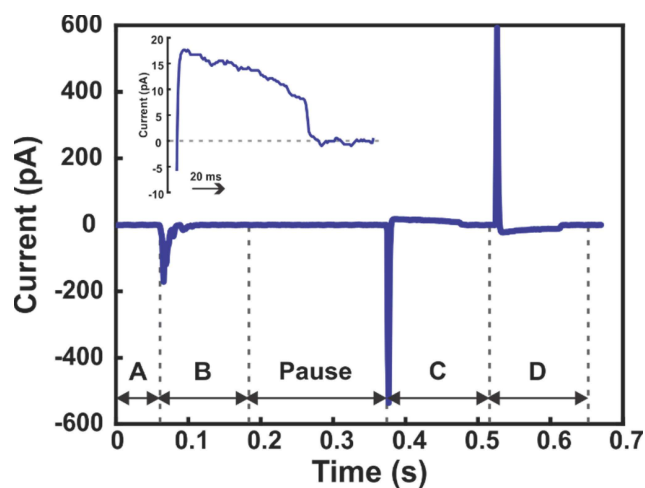

Figure 6. Tip current trace during a single pixel of a simultaneous topographical and electrochemical activity map. The tip approach (A), short tip retract (B), pause, electrochemical pulse (C) and large tip retract (D) correspond to the stages labelled as in Figure 1b, c, d. Tip potential: 0.4 V, substrate potential pulsed from 0 V to −0.7 V (C), but otherwise 0 V. Insert: magnified I vs. t trace for section C.

immediately withdraws from the surface by a defined amount and the current consequently decreases to zero (B). After a wait period, the potential at the substrate is jumped cathodically to drive HER, and after a cathodic spike in the tip current, attributed to coupling between the tip and substrate through the interelectrode capacitance and resistance,[3] an anodic current flows at the tip electrode indicative of H_2 detection (C).

Electrochemical images were obtained by averaging different intervals of the tip current during this period (*vide infra*). When the potential at the substrate is reversed, the current at the tip quickly returns to zero (D), again after an anodic spike, indicative of electronic coupling of the (large) substrate response in the tip response.

The insert in Figure 6 shows the current trace profile during the substrate potential pulse period. The oxidation current decays steadily and further drops to near zero after approx. 80 ms into the potential pulse. Analysis of the form of the curve is complicated by the very close tip-substrate separation, on a scale where geometrical effects (including non-ideal tip-substrate geometry) and electric field effects may impact mass transport and local concentrations.[61,63]

Figure 7 displays simultaneous topography and SECM data recorded over the Au nanocrystal, compared with an SEM image of the same crystal (a). The topographical map (b) is in good agreement with the SEM image and the electrochemical maps (c and d). The slight offset between the topography map and electrochemical images is attributed to some asymmetry in the tip geometry.[64] The electrochemical maps show a clear increase in tip current (hydrogen oxidation) over the Au nanocrystal, with a diffusional decay in the region beyond, indicating the higher activity of the Au substrate for HER. Figure 7c was constructed by averaging the first 30 ms of anodic tip current during the substrate potential pulse period, while Figure 7d which was constructed by averaging the tip current during the last 30 ms of the substrate potential pulse
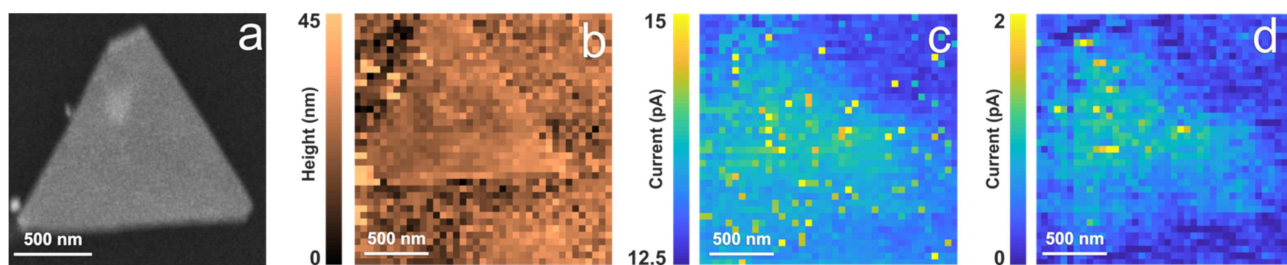
Figure 7. a) SEM image of an Au nanocrystal. Simultaneous topography b) and SECM scan of the same crystal in 0.1 M HClO$_4$. Approach velocity: 400 nm s^{-1}. Tip bias: 0.4 V (substrate potential 0 V). First retract: 16 nm. Pause: 0.15 s. Substrate potential pulsed from 0 V to −0.7 V for 0.15 s with electrochemical maps taken from the average of c) the first 30 ms period after the pulse with anodic current and d) last 30 ms of the pulse. Second retract: 70 nm and move to next point. Current set point: 50 pA. Pixel size: 50 nm. A simple in-painting protocol (described in the text) was used for redundant pixels where there was tip-substrate contact during the period of interest (the raw data are shown in the Supporting Information, Figure S7). Total scan time = 23 minutes.

period. For redundant pixels, where there was tip contact with the sample during the analysis period (*vide infra*), a simple "in-painting" method was employed using an average of the previous and subsequent pixel (the images without this procedure are shown in the Supporting Information, Figure S7a and b. It is noteworthy that the background electrochemical current is on the pA scale, which is much lower than the leakage current of most previous in-situ electrochemical STM studies, typically in the range 10 s–100 s pA.[34,65] This demonstrates the considerable advantage of using nanoelectrodes sealed in quartz as the tip.

As with the ambient scans (Figure 5), there is a tip overshoot as displayed in the approach curve in Figure 8a. In this case, the slower approach rate and faster data acquisition allowed more data points to be acquired during the tip approach and reduced the amount of overshoot (estimated in the same way as described for Figure 5a), with the majority of approaches stopping within an estimated 0.5 nm of the threshold (Figure 8b). The contact pixels occurred more commonly over the Au crystals than the GC support (Supporting Information, Figure S7). This could potentially be due to differences in the conductance and work function of the Au crystal and GC. As GC has a smaller work function, the STM (tunnelling current) – distance approach curve would be shallower,[66,67]

meaning that the system would have more time to "react" to the increase in tunnelling current during the tip approach. The occurrence of contact pixels increased significantly when shorter retract distances after the initial approach were used. This would appear to support the argument presented above that there could be a more significant overshoot (than expected from the data in Figure 8a) due to the inherent piezoelectric positioner response, which results in the tip remaining in contact with the surface, even when a short retraction distance is applied. The two main factors determining the frequency of the observed contact pixels is the initial approach rate and the retract distance, as summarised in Figure 9 for 32 different experimental scans. Unfortunately, a consequence of reducing the tip approach rate is that the length of time taken to complete scans is greatly increased which could result in other issues, such as thermal drift and contamination of the tip and sample.

4. Conclusions

In this paper we have implemented C- and T-SECM measurements of electrode surfaces, enabling synchronous maps of substrate topography and electroactivity. The use of a hopping
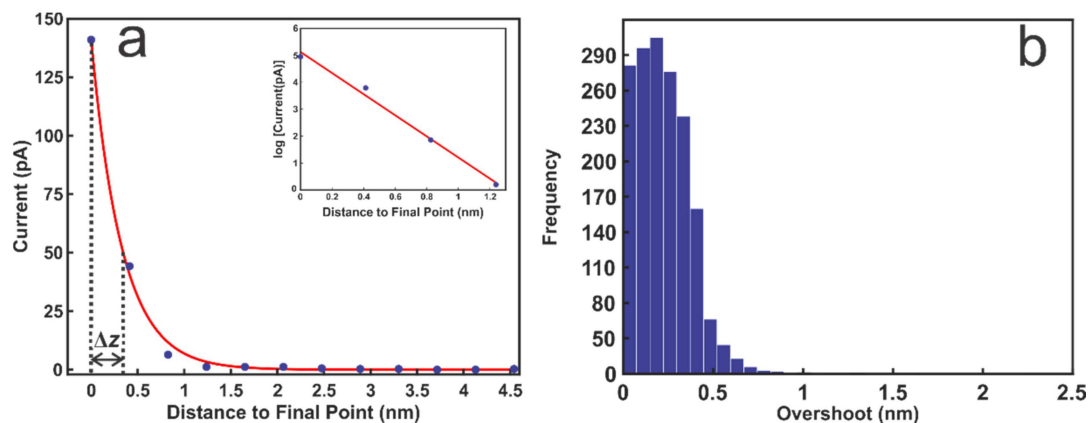

Figure 8. a) Typical approach curve taken from the scan in Figure 7b, plotted using the tip current, approach rate (400 nm s^{-1}) and time; the position overshoot, Δz, marked and calculated as explained in the text. Inset shows linear semi-log current-distance analysis. b) Histogram of calculated overshoot values for all tip approaches in Figure 7b. Total histogram count: 1638.
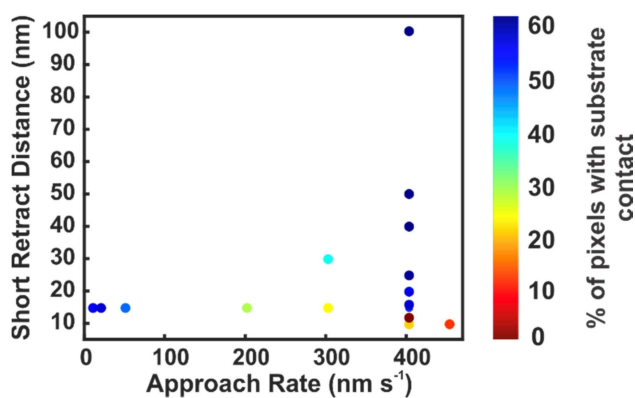
Figure 9. Percentage of pixels for which there is tip-substrate contact during the electrochemical pulse phase of C-SECM scans, depending on both approach rate and the short retract distance. Data taken from 32 different scans with both GC and Au nanocrystals deposited.

mode imaging protocol sought to address issues around piezoelectric positioner instability and noise. We have illustrated the capability of this approach by imaging the topography of electrode substrates with large topographical features in air, with a conventional Pt/Ir cut wire STM tip and for electrodes in solution with a carbon nanoelectrode tip sensitised with Pt. The latter is particularly useful for in-situ electrochemical STM measurements as the background current level (noise) is very low. In the hopping mode protocol, the tip is approached to the surface at a series of predefined pixels across the surface and the tip position stops and the topography is sensed when a certain current (tunnelling or conductance) is exceeded. The approach parameters can be set to minimise tip-substrate contact, although there are consequences for the approach rates and timeframe of measurements. A retraction of the tip allows subsequent SECM measurements, but for short tip retraction there are some issues with tip-surface contact. This study has highlighted the conditions for successful topography-activity measurements with C-SECM and with the information herein there are prospects for using this type of approach for future STM-SECM measurements. Although we have been able to implement C- and T-SECM on a conventional SEPM platform, an STM positioning system would be most appropriate for studies at high resolution.

Data Accessibility Statement

All data present in this manuscript can be found at the Warwick Research Archive Portal http://wrap.warwick.ac.uk/132201. These data are provided free of charge.

Acknowledgements

[1] G. Binning, H. Rohrer, C. Gerber, E. Weibel, *Phys. Rev. Lett.* **1982**, *49*, 57–61.
[2] L. Jacobse, Y. F. Huang, M. T. M. Koper, M. J. Rost, *Nat. Mater.* **2018**, *17*, 277–282.
[3] A. J. Bard, F. R. F. Fan, J. Kwak, O. Lev, *Anal. Chem.* **1989**, *61*, 132–138.
[4] N. Ebejer, A. G. Güell, S. C. S. Lai, K. McKelvey, M. E. Snowden, P. R. Unwin, *Annu. Rev. Anal. Chem.* **2013**, *6*, 329–351.
[5] R. C. Engstrom, M. Weber, D. J. Wunder, R. Burgess, S. Winquist, *Anal. Chem.* **1986**, *58*, 844–848.
[6] G. Binnig, C. F. Quate, C. Gerber, *Phys. Rev. Lett.* **1986**, *56*, 930–933.
[7] J. H. K. Pfisterer, Y. Liang, O. Schneider, A. S. Bandarenka, *Nature* **2017**, *549*, 74–77.
[8] F. P. Zamborini, R. M. Crooks, *Langmuir* **1997**, *13*, 122–126.
[9] N. Tao, C. Li, H. He, *J. Electroanal. Chem.* **2000**, *492*, 81–93.
[10] M. Kang, D. Momotenko, A. Page, D. Perry, P. R. Unwin, *Langmuir* **2016**, *32*, 7993–8008.
[11] Y. Takahashi, A. Kumatani, H. Shiku, T. Matsue, *Anal. Chem.* **2017**, *89*, 342–357.
[12] C. Kranz, *Analyst* **2014**, *139*, 336–52.
[13] C. L. Bentley, J. Edmondson, G. N. Meloni, D. Perry, V. Shkirskiy, P. R. Unwin, *Anal. Chem.* **2019**, *91*, 84–108.
[14] M. Kang, D. Perry, C. L. Bentley, G. West, A. Page, P. R. Unwin, *ACS Nano* **2017**, *11*, 9525–9535.
[15] D.-Q. Liu, B. Tao, H.-C. Ruan, C. L. Bentley, P. R. Unwin, *Chem. Commun.* **2019**, *55*, 628–631.
[16] A. Page, M. Kang, A. Armitstead, D. Perry, P. R. Unwin, *Anal. Chem.* **2017**, *89*, 3021–3028.
[17] A. J. Bard, M. V. Mirkin, *Scanning Electrochemical Microscopy*, CRC Press **2012**.
[18] T. Kai, C. G. Zoski, A. J. Bard, *Chem. Commun.* **2018**, *54*, 1934–1947.
[19] J. Rheinlaender, N. A. Geisse, R. Proksch, T. E. Schäffer, *Langmuir* **2011**, *27*, 697–704.
[20] J. V. Macpherson, P. R. Unwin, *Anal. Chem.* **2000**, *72*, 276–285.
[21] J. Meier, K. A. Friedrich, U. Stimming, *Faraday Discuss.* **2002**, *365–372*, discussion 441–462.
[22] T. H. Treutler, G. Wittstock, *Electrochim. Acta* **2003**, *48*, 2923–2932.
[23] C. Kranz, G. Friedbacher, B. Mizaikofft, A. Lugstein, E. Bertagnolli, *Anal. Chem.* **2001**, *73*, 2491–2500.
[24] Z. Huang, P. De Wolf, R. Poddar, C. Li, A. Mark, M. R. Nellist, Y. Chen, J. Jiang, G. Papastavrou, S. W. Boettcher, C. Xiang, B. S. Brunschwig, *Microsc. Today* **2016**, *24*, 18–25.
[25] M. R. Nellist, Y. Chen, A. Mark, S. Gödrich, C. Stelling, J. Jiang, R. Poddar, C. Li, R. Kumar, G. Papastavrou, M. Retsch, B. S. Brunschwig, Z. Huang, C. Xiang, S. W. Boettcher, *Nanotechnology* **2017**, *28*, 095711.
[26] D. J. Comstock, J. W. Elam, M. J. Pellin, M. C. Hersam, *Anal. Chem.* **2010**, *82*, 1270–1276.
[27] Y. Takahashi, A. I. Shevchuk, P. Novak, Y. Murakami, H. Shiku, Y. E. Korchev, T. Matsue, *J. Am. Chem. Soc.* **2010**, *132*, 10118–10126.
[28] B. Ballesteros Katemann, A. Schulte, W. Schuhmann, *Chem. Eur. J.* **2003**, *9*, 2025–2033.
[29] A. Page, D. Perry, P. Young, D. Mitchell, B. G. Frenguelli, P. R. Unwin, *Anal. Chem.* **2016**, *88*, 10854–10859.
[30] Y. Takahashi, A. I. Shevchuk, P. Novak, B. Babakinejad, J. Macpherson, P. R. Unwin, H. Shiku, J. Gorelik, D. Klenerman, Y. E. Korchev, T. Matsue, *Proc. Proc. Natl. Acad. Sci.* **2012**, *109*, 11540–11545.
[31] O. Sklyar, T. H. Treutler, N. Vlachopoulos, G. Wittstock, *Surf. Sci.* **2005**, *597*, 181–195.
[32] M. S. Ramachandra Rao, G. Margaritondo, *J. Phys. D* **2011**, *44*, 460301.
[33] A. Schulte, *Proc. SPIE-Int. Soc. Opt. Eng.* **1998**, *3512*, 353–357.
[34] C. E. Bach, R. J. Nichols, W. Beckmann, H. Meyer, *J. Electrochem. Soc.* **1993**, *140*, 1281.
[35] L. A. Nagahara, T. Thundat, S. M. Lindsay, *Rev. Sci. Instrum.* **1989**, *60*, 3128–3130.

[36] M. V. Mirkin, T. Sun, Y. Yu, M. Zhou, *Acc. Chem. Res.* **2016**, *49*, 2328–2335.

[37] T. Sun, D. Wang, M. V. Mirkin, *Angew. Chem. Int. Ed.* **2018**, *57*, 7463–7467; *Angew. Chem.* **2018**, *130*, 7585–7589.

[38] T. Sun, D. Wang, M. V. Mirkin, *Faraday Discuss.* **2018**, *210*, 173–188.

[39] C. L. Bentley, P. R. Unwin, *Faraday Discuss.* **2018**, *210*, 365–379.

[40] R. M. Penner, M. J. Heben, T. L. Longin, N. S. Lewis, *Science* **1990**, *250*, 1118–1121.

[41] A. G. Güell, I. Díez-Pérez, P. Gorostiza, F. Sanz, *Anal. Chem.* **2004**, *76*, 5218–5222.

[42] P. Wilde, T. Quast, H. B. Aiyappa, Y.-T. Chen, A. Botz, T. Tarnev, M. Marquitan, S. Feldhege, A. Lindner, C. Andronescu, W. Schuhmann, *ChemElectroChem* **2018**, *5*, 3083–3088.

[43] Y. Takahashi, A. I. Shevchuk, P. Novak, Y. Zhang, N. Ebejer, J. V. Macpherson, P. R. Unwin, A. J. Pollard, D. Roy, C. A. Clifford, H. Shiku, T. Matsue, D. Klenerman, Y. E. Korchev, *Angew. Chem. Int. Ed.* **2011**, *50*, 9638–9642; *Angew. Chem.* **2011**, *123*, 9812–9816.

[44] M. Şen, Y. Takahashi, Y. Matsumae, Y. Horiguchi, A. Kumatani, K. Ino, H. Shiku, T. Matsue, *Anal. Chem.* **2015**, *87*, 3484–3489.

[45] I. M. Ornelas, P. R. Unwin, C. L. Bentley, *Anal. Chem.* **2019**, *91*, 14854–14859.

[46] N. M. Andoy, X. Zhou, E. Choudhary, H. Shen, G. Liu, P. Chen, *J. Am. Chem. Soc.* **2013**, *135*, 1845–1852.

[47] M. Sastry, A. Rai, *Nat. Mater.* **2004**, *3*, 482.

[48] A. G. Güell, A. S. Cuharuc, Y.-R. Kim, G. Zhang, S. Tan, N. Ebejer, P. R. Unwin, *ACS Nano* **2015**, *9*, 3558–3571.

[49] Warwick Electrochemisitry and Interfaces Group, "WEC-SPM," can be found under https://warwick.ac.uk/fac/sci/chemistry/research/unwin/electrochemistry/wec-spm/ **2019**.

[50] J. Kim, M. Shen, N. Nioradze, S. Amemiya, *Anal. Chem.* **2012**, *84*, 3489–3492.

[51] T. Sun, Y. Yu, B. J. Zacher, M. V Mirkin, *Angew. Chem. Int. Ed. Engl.* **2014**, *53*, 14120-3.

[52] J. V. Macpherson, P. R. Unwin, *Anal. Chem.* **1997**, *69*, 2063–2069.

[53] P. Novak, A. Shevchuk, P. Ruenraroengsak, M. Miragoli, A. J. Thorley, D. Klenerman, M. J. Lab, T. D. Tetley, J. Gorelik, Y. E. Korchev, *Nano Lett.* **2014**, *14*, 1202–1207.

[54] F. Kalkan, C. Zaum, K. Morgenstern, *Rev. Sci. Instrum.* **2012**, *83*, 103903.

[55] L. Petersen, M. Schunack, B. Schaefer, T. R. Linderoth, P. B. Rasmussen, P. T. Sprunger, E. Laegsgaard, I. Stensgaard, F. Besenbacher, *Rev. Sci. Instrum.* **2001**, *72*, 1438–1444.

[56] Physik Intrumente LTD UK, "P-753 LISA Linear Actuator and Stage," can be found under https://www.physikinstrumente.com/en/products/nanopositioning-piezo-flexure-stages/linear-piezo-flexure-stages/p-753-lisa-linear-actuator-stage-200900/ **2019**.

[57] Physik Intrumente LTD UK, "P-620.Z - P-622.Z PIHera Vertical Precision Z Positioner," can be found under https://www.physikinstrumente.com/en/products/nanopositioning-piezo-flexure-stages/linear-piezo-flexure-stages/p-620z-p-622z-pihera-precision-z-stage-202501/ **2019**.

[58] S. S. Shankar, A. Rai, B. Ankamwar, A. Singh, A. Ahmad, M. Sastry, *Nat. Mater.* **2004**, *3*, 482–488.

[59] A. Avila, B. Bhushan, *Crit. Rev. Solid State Mater. Sci.* **2010**, *35*, 38–51.

[60] M. Lanza, *Conductive Atmoic Force Microscopy: Applications in Nano-materials* **2017**.

[61] J. Perez, E. R. Gonzalez, H. M. Villullas, *J. Phys. Chem. B* **1998**, *102*, 10931–10935.

[62] L. Zhang, J. Xiao, H. Wang, M. Shao, *ACS Catal.* **2017**, *7*, 7855–7865.

[63] M. A. Edwards, H. S. White, H. Ren, *ACS Nano* **2019**, *13*, 6330–6340..

[64] B. Uluutku, M. Z. Baykara, J. Vac, *Sci. Technol. B, Nanotechnol. Micro-electron. Mater. Process. Meas. Phenom.* **2015**, *33*, 031802.

[65] Z. F. Chen, E. Wang, *Electroanalysis* **1994**, *6*, 672–676.

[66] A. D. Gottlieb, L. Wesoloski, *Nanotechnology* **2006**, *17*, R57–R65.

[67] J. Polesel-Maris, C. Lubin, F. Thoyer, J. Cousty, *J. Appl. Phys.* **2011**, *109*, 74320.